Synthesis of hierarchical sulfonated graphene/MnO$_2$/polyaniline ternary composite and its improved electrochemical performance

Guangxiang Wang, Qianqiu Tang, Hua Bao, Xingwei Li, Gengchao Wang*

Key Laboratory for Ultrafine Materials of Ministry of Education, Shanghai Key Laboratory of Advanced Polymeric Materials, School of Materials Science and Engineering, East China University of Science and Technology, P.O. Box 289, 130 Meilong Rd., Shanghai 200237, PR China

HIGHLIGHTS

- The MnO$_2$/PANI nanoparticles with 5–10 nm were uniformly deposited onto sulfonated graphene nanosheets.
- Ternary composite shows high electrical conductivity and surface area compared to MnO$_2$/PANI.
- Ternary composite exhibits superior rate capability and excellent cycling stability.

ARTICLE INFO

ABSTRACT

A novel ternary composite of sulfonated graphene/MnO$_2$/polyaniline (sGMOPANI) is synthesized via a dilute in-situ polymerization method using potassium permanganate as oxidant under neutral condition. The FE-SEM and HRTEM images show that MnO$_2$/polyaniline nanoparticles with the diameter of 5–10 nm deposit onto sulfonated graphene nanosheets. Spectral analysis reveals the existence of the hydrogen bond and π–π interaction between MnO$_2$/polyaniline nanoparticles and sulfonated graphene. As a result, the sGMOPANI composite based on the two-electrode cell shows improved electrochemical capacitance (276 F g^{-1} at 1 g^{-1} in 1 M Na$_2$SO$_4$), better rate capability (73% capacitance retention from 0.2 to 20 A g^{-1}), and higher cycling stability (11.7% capacitance loss after 3000 cycles) compared to the MnO$_2$/polyaniline binary composite.

1. Introduction

With increased sustainable energy production from solar and wind or other renewable energy sources, high efficiency energy-storage systems have stimulated intense research interest in areas such as batteries and supercapacitors [1–3]. Supercapacitors have attracted much attention as energy-storage devices due to their high power density, faster power delivery, long cycle life compared to secondary batteries [4,5]. However, supercapacitors often provide lower energy density than batteries. Therefore, it is necessary to improve their energy performance and reduce fabrication costs for extensive applications including energy-storage systems, hybrid vehicles, consumer electronics, memory back-up systems, and industrial power management [1,6].

In order to improve the energy performance of supercapacitors, most of works are focused on searching innovative electrode materials, including carbonaceous materials [7–9], conducting polymers [10,11] and transition-metal oxides [12–14]. Among them, MnO$_2$ is considered to be a prospective material for the supercapacitors due to its low cost, natural abundance, environmental benignity and high theoretical specific capacitance (SC) of 1370 F g^{-1} [15,16]. However, densely packed structure and poor electrical conductivity of MnO$_2$ severely limit its practical capacitance [17]. To overcome the agglomeration problem of MnO$_2$ and effectively utilize MnO$_2$ materials, nanostructured MnO$_2$ [18–24] with intrinsically large surface area has been investigated widely, showing improved electrochemical performance. For instance, Jiang [23] synthesized ultrafine MnO$_2$ nanowires with sub-10 nm diameters by a simple hydrothermal method, followed by subsequent calcinations to form networks, achieving an enhanced specific capacitance, high rate capability and good cycling stability. On the other hand, it was found that MnO$_2$ combined with conductive electrode materials, such as activated

carbon [25], CNTs [26–30], graphene [31–35], PANI [36–40], PPy [41,42], and PEDOT [43,44], etc., can improve electrical conductivity of MnO_2. Most recently, to get better electrochemical performance with each component providing much needed function for efficient use of MnO_2 for energy storage, ternary composites of MnO_2 with carbon materials and conducting polymers [17,45–50] have gained much attention. Li et al. [47] fabricated multi-walled carbon/polyaniline/MnO_2 ternary coaxial structures through a simple wet chemical method, providing large surface area and decreasing the contact resistance between different components, so intriguing electrochemical properties are achieved. Wang et al. [49] prepared hierarchical MnO_2/conducting polypyrrole@carbon nanofiber triaxial nano-cables via in-situ interfacial redox reaction. With such unique structure, the composite exhibits a high specific capacitance (705 F g^{-1}), as well as good rate capability and cycling stability. These studies demonstrated that the combination of MnO_2 and conductive components at nano-scale level can greatly improve the electrochemical performance of ternary composites.

Graphene, a two-dimensional sp^2-bonded carbon with extraordinary electrical conductivity and mechanical properties, has gained considerable interest [9,51]. More importantly, graphene can provide high loading of MnO_2 with nano-scale due to its large accessible surface area [52,53]. However, to our knowledge, there have been no reports on hierarchical graphene/MnO_2/PANI ternary composites so far.

In this research, we report a novel strategy to synthesize hierarchical sulfonated graphene/MnO_2/PANI (sGMOPANI) ternary composite by a dilute in-situ polymerization method. In our method, we concentrate on the synergistic effect from the combination of graphene, MnO_2, and PANI in ternary composite to effectively utilize each component. In order to prevent the aggregation of graphene nanosheets in aqueous solution, sulfonated graphene nanosheets (sGNS) were used as the substrates. During synthesis process, aniline monomers were oxidative polymerized by $KMnO_4$ while $KMnO_4$ was reduced to MnO_2. Furthermore, MnO_2/PANI composite nanoparticles were deposited onto the surface of sGNS and the sGMOPANI ternary composite was fabricated. The resulting sGMOPANI composite not only exhibited high electrochemical capacitance of MnO_2 and PANI, but also maintained the advantage of excellent rate capability and cycling stability of sGNS.

2. Experimental

2.1. Fabrication of sulfonated graphene/MnO_2/polyaniline composite

The sulfonated graphene nanosheets (sGNS) were prepared using the method described in the literatures [54,55]. Hierarchical sGNS/MnO_2/PANI ternary composite (sGMOPANI) was synthesized by dilute in-situ polymerization method. Typical procedure was as follows: 70 mg of sGNS was homogeneously dispersed in 300 mL of deionized water and acetone mixture solution (10/90, v/v %) with ultrasonication for 30 min. Then 0.47 g of aniline was added into the above solution and stirred for 30 min at 0 °C to form a uniform mixture. 0.37 g of $KMnO_4$ was dissolved in 50 mL of deionized water at 0 °C, and then was added dropwise into the above mixture for 15 min. The reaction was allowed to continue for 48 h at 0 °C under continuous stirring. sGMOPANI composite was obtained by centrifugation of the resulting dispersion, washing with deionized water and ethanol, followed by freeze drying. For comparison, MnO_2/PANI (MOPANI) binary composite was synthesized through the similar procedure above without the presence of sGNS.

2.2. Materials characterization

Fourier-transform infrared (FTIR) spectra were obtained through a Nicolet 5700 spectrometer using KBr pallets. Raman spectra were recorded with Renishaw in Via + Reflex using a 50 mW He–Ne laser operated at 515 nm. X-ray photoelectron spectroscopy (XPS) spectra were recorded with a thermo scientific ESCALAB 250Xi X-ray photoelectron spectrometer equipped with amonochromatic Al Kα X-ray source (1486.6 eV). The morphologies of the as-prepared samples were observed by field-emission scanning electron microscope (FE-SEM, Hitachi S-4800) and high-resolution transmission electron microscope (HRTEM, JEOL JEM-2100). Powder X-ray diffraction (XRD) patterns were performed in a Rigaku D/Max 2550 VB/PC X-ray diffractometer using Cu (Kα) radiation with the 2θ-angle recorded from 5 to 75°. Nitrogen adsorption–desorption isotherms were performed using a Micromeritics ASAP 2020 analyzer at 77 K. The electrical conductivity of the samples was determined using an SX 1934 four-probe instrument.

2.3. Electrochemical measurements

The working electrodes were prepared by dispersing 75 wt% of active materials, 20 wt% of acetylene black and 5 wt% of poly(-tetrafluoroethylene) (PTFE) binder in a mixed solution of deionized water and ethanol (1/10, by volume) to form a homogenous slurry. The slurry was rolled and then pressed onto the titanium mash. The cell supercapacitors were composed of two symmetrical working electrodes sandwiched by a separator and the aqueous electrolyte solution of 1 M Na_2SO_4.

Cyclic voltammetry (CV) and electrochemical impedance spectroscopy (EIS) measurements were performed on a CHI 660D electrochemical workstation in a three-electrode mode using the as-prepared samples, an Ag/AgCl (KCl saturated) electrode, and Pt as the working electrode, reference electrode and counter electrode, respectively. Galvanostatic charge–discharge tests of the cell supercapacitors were conducted on a LAND CT2001A program testing system in a two-electrode mode. The potential range for CV tests was 0–0.7 V and the scan rate was 2–100 mV s^{-1}. The potential range for charge/discharge tests was 0–0.7 V. EIS measurements were carried out in the frequency range of 10^5–0.01 Hz at 5 mV amplitude referring to open circuit potential.

The specific capacitance of the electrode materials can be calculated from the CVs according to the equation: $C = \int IdV/vmV$, where C (F g^{-1}) is specific capacitance, I is the output current (A), V is the potential (V), v is the potential scanning rate (mV s^{-1}) and m is the mass of the active material in the electrodes (g). The specific capacitance (C) of the active electrode materials was also determined from the charge/discharge curves using the equation: $C = (I\Delta t)/(m\Delta V)$, where I is discharge current, Δt is the discharging time, m the mass of active electrode materials on single side, and ΔV is the voltage drop upon discharging (excluding the *IR* drop).

3. Results and discussion

FTIR spectra for sGNS, MOPANI and sGMOPANI are shown in Fig. 1(A). The spectrum of sGNS indicates the presence of C=C ($v_{C=C}$ at 1565 cm^{-1}) and –SO_3H ($v_{O=S=O}$ at 1033 and 1003 cm^{-1}). For MOPANI, the strong peak at around 528 cm^{-1} is attributed to Mn–O stretching vibration, which confirms the presence of a large amount of MnO_2. And three peaks at 1559, 1473, and 1102 cm^{-1} are assigned to characteristic absorption of PANI, corresponding to the C=C stretching vibrations of the quinoid and benzenoid rings, and C–H in plane bending vibration, respectively. In addition, the peak at 1610 cm^{-1} is ascribed to N–H stretching vibration, indicating that the MOPANI contains –NH_2 groups, namely, there are
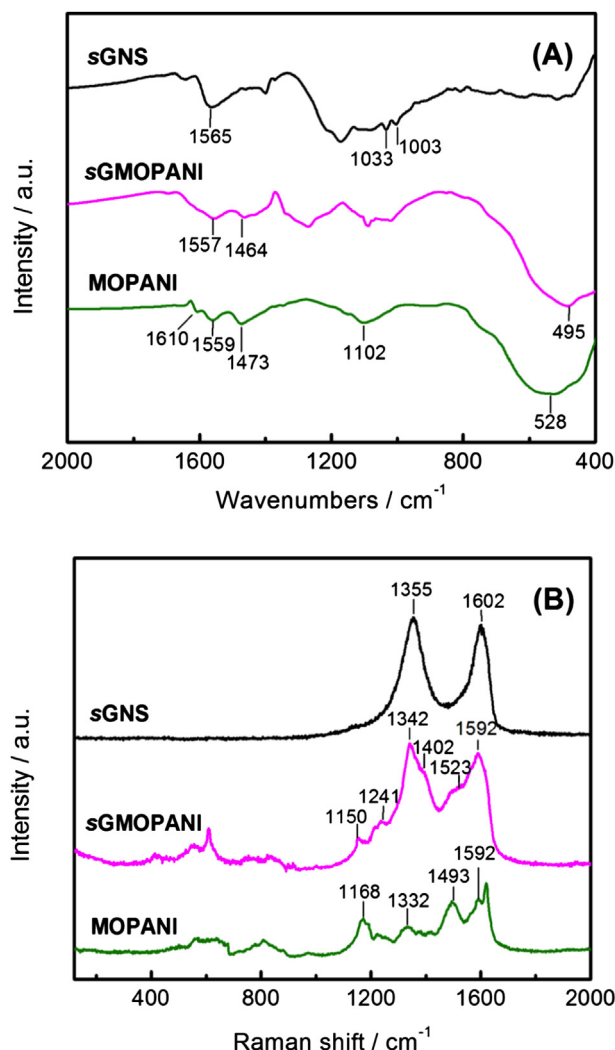
Fig. 1. (A) FTIR and (B) Raman spectra of sGNS, MOPANI, and sGMOPANI.

sGMOPANI, the X-ray photoelectron spectroscopy analysis is employed. As shown in Fig. 2(A), Both MOPANI and sGMOPANI display C 1s, N 1s, O 1s and Mn 2p peaks, indicating the existence of PANI and manganese oxide components. The additional peak of S 2p in sGMOPANI spectrum illustrates the introduction of sGNS. The Mn 2p spectra for MOPANI and sGMOPANI are presented in Fig. 2(B). The peaks centered at 653.8 eV and 642 eV corresponding to Mn $2p_{1/2}$ and Mn $2p_{3/2}$, respectively, with spin energy separation of 11.8 eV, consistent with the previous data for MnO_2 [56,57]. The element content and chemical composition of MOPANI and sGMOPANI are calculated from the XPS survey spectra (Table 1). The MnO_2/PANI mass ratio is 71/29 in MOPANI while the MnO_2/PANI/sGNS mass ratio is 45/31/24 in sGMOPANI. It is apparent that sGMOPANI has more relative amount of PANI compared with MOPANI under same feed mass ratio of aniline/$KMnO_4$, which suggests that the introduction of sGNS contributes to the growth of PANI.

The O 1s deconvolution XPS spectra for MOPANI and sGMOPANI are analyzed by curve fitting. The O 1s deconvolution spectra of MOPANI exhibit two components of the oxygen bond at 529.8 eV (Mn–O–Mn) and 531 eV (Mn–OH) (Fig. 2(C)). For sGMOPANI, the spectrum reveals the presence of three oxygen bonding configurations, including Mn–O–Mn (530 eV), Mn–OH (531.2 eV) and additional O–H (533.5 eV) (Fig. 2(D)). The additional O–H may be attributed to $-SO_3^-$ and hydroxyl groups of sGNS. It is also noted that the relative peak area of Mn–OH in sGMOPANI is bigger than that of MOPANI, which is probably ascribed to the hydrogen bonds between MnO_2 and the $-SO_3H$ and hydroxyl groups of sGNS.

The morphologies of the MOPANI and sGMOPANI are characterized by the FE-SEM and HRTEM. As shown in Fig. 3a and c, MOPANI exhibits an evidently aggregated structure composed of many MOPANI nanoparticles with the diameter of 5–10 nm (marked in Fig. 3c). The aggregation is most likely formed through the following reaction process. Firstly, aniline is polymerized by $KMnO_4$ as oxidant and $KMnO_4$ itself is reduced to MnO_2. Then, MnO_2/PANI nanoparticles are formed by non-covalent interaction. Furthermore, MnO_2/PANI nanoparticles tend to aggregate to larger particles. In contrast, FE-SEM image of sGMOPANI illustrates those MnO_2/PANI composite nanoparticles with the diameter of 5–10 nm deposit uniformly onto the surface of sGNS (Fig. 3b). HRTEM image further indicates that the diameter of MnO_2/PANI nanoparticles is 5–10 nm (Fig. 3d). In this case, the introduction of aqueous dispersed sGNS with large surface area provides a substrate to the deposition of MnO_2/PANI nanoparticles, thus preventing the further agglomeration of MnO_2/PANI nanoparticles.

The energy dispersive spectroscopic (EDS) mapping/imaging analysis of sGMOPANI is demonstrated in Fig. 4. Fig. 4a–d exhibits the elemental distribution of C, N, Mn and O in sGMOPANI composite, revealing the presence of the sGNS, PANI and MnO_2. The mapping results also indicate that the distribution of Mn, O and N is homogenous in the whole region, further confirming the uniform distribution of MnO_2/PANI nanoparticles on the surface of sGNS.

Fig. 5 shows XRD patterns of sGNS, MOPANI and sGMOPANI. For sGNS, a broad (002) diffraction peak at 2θ between 15 and 35° is observed, resulting from a disordered stacking of sulfonated graphene nanosheets. Both MOPANI and sGMOPANI exhibit three weak diffraction peaks at $2\theta = 12.7°$ (110), 37.2° (211) and 65.7° (002) indexed to α-MnO_2 (JCPDS No. 44-0141) [58]. This indicates that the as-prepared MOPANI and sGMOPANI has poor crystallinity of α-MnO_2 [59], which is because the amorphous PANI deposits onto the surface of α-MnO_2 and orderly growth of α-MnO_2 crystals is restricted. Besides, the sGMOPANI displays a low and broad peak at 2θ between 20 and 30° corresponding to sGNS.

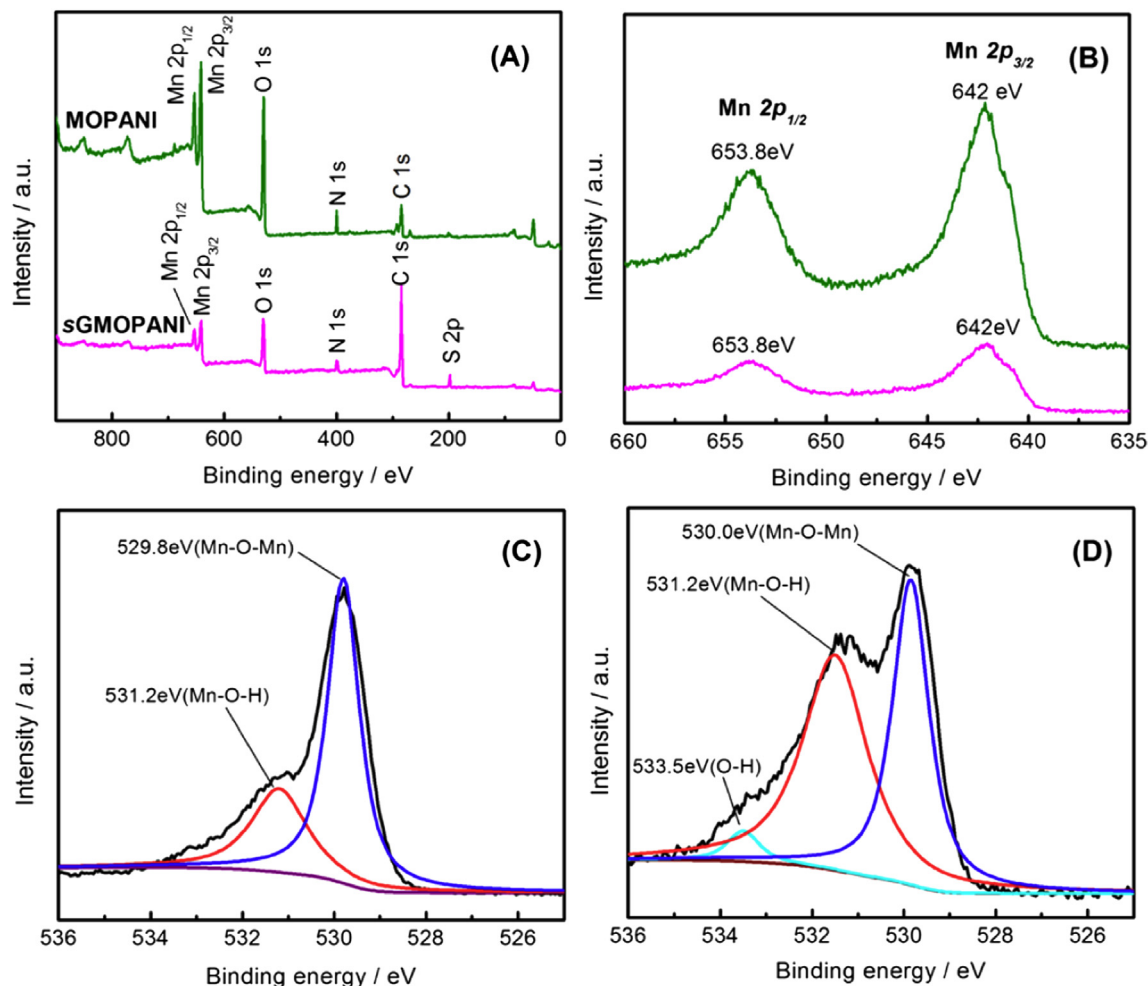Fig. 6(A) shows the N_2 adsorption/desorption isotherms of MOPANI and sGMOPANI at 77 K. The sGMOPANI exhibits obvious

oligomers of aniline in MOPANI. In sGMOPANI composite, the peak at 1610 cm^{-1} disappears, revealing no oligomers of aniline in the composite. Meanwhile, characteristic peaks corresponding to PANI (1557 and 1464 cm^{-1}) and MnO_2 (495 cm^{-1}) also appear in sGMOPANI. Furthermore, the characteristic peaks corresponding to PANI and MnO_2 in sGMOPANI red-shift compared with MOPANI. This is probably ascribed to the π–π electronic interaction between PANI and the basal plane of sGNS, the doping effect of $-SO_3H$ groups in sGNS on PANI, as well as the hydrogen bonding between MnO_2 and sGNS.

Fig. 1(B) presents the Raman spectra of sGNS, MOPANI and sGMOPANI. The Raman spectrum of the sGNS shows two intense bands at 1602 and 1355 cm^{-1}, corresponding to the G band and the D band of sGNS, respectively. For MOPANI, the absorption band in 570–650 cm^{-1} region is attributed to Mn–O stretching vibration, and the bands at 1592, 1493, 1332 and 1168 cm^{-1} are ascribed to PANI characteristic absorption. The sGMOPANI exhibits the characteristic bands corresponding to sGNS (1592 and 1342 cm^{-1}), PANI (1523 and 1402 cm^{-1}) and MnO_2 (480–680 cm^{-1}). It is also found that the characteristic bands of sGNS and PANI in sGMOPANI shift to lower wavenumbers compared with MOPANI, which is in good accordance with our FTIR results above.

To determine the chemical composition and to further investigate the interaction between various components in MOPANI and

Fig. 2. XPS spectra of MOPANI and sGMOPANI. (A) Wide scan survey spectra, (B) Mn *2p* XPS spectra, O *1s* core level XPS spectra for (C) MOPANI and (D) sGMOPANI.

hysteresis loops with capillary condensation with a BET surface area of 97 m^2 g^{-1}. In contrast, the hysteresis loop of MOPANI almost disappears and its surface area decreases to 13 m^2 g^{-1}. The larger specific area of sGMOPANI is due to the introduction of sGNS with good aqueous dispersion, which provides a substrate to the deposition of MnO$_2$/PANI nanoparticles and prevents them from further agglomerating. From Fig. 6(B), it is identified that the pore size of sGMOPANI is broadly distributed in the mesoporous region of 10–20 nm, while MOPANI has a narrow pore size distribution around 2.5 nm. In conclusion, more applicable mesoporous distribution and larger specific area is achieved for sGMOPANI, so it is expected that sGMOPANI may exhibit improved electrochemical performance compared to MOPANI.

As is known to all, sGNS has exceptional conductivity compared to MnO$_2$, so the introduction of sGNS is expected to enhance the conductivity of sGMOPANI. The electrical conductivity of MOPANI is very low ($<1 \times 10^{-8}$ S cm^{-1}), exhibiting electrical insulating property. The conductivity of sGMOPANI reaches a value of

0.035 S cm^{-1}, which is over 10^6 times higher than that of MOPANI. This is favorable to improve the electrochemical performance of sGMOPANI.

In order to evaluate the contribution of sGNS to the electrochemical performance of the electrode materials, cyclic voltammetry (CV), galvanostatic charge–discharge and electrochemical impedance spectroscopy (EIS) measurements in a three-electrode system were employed. Fig. 7(A) and (B) shows the cyclic voltammograms of MOPANI and sGMOPANI with various scanning rates. Both CVs of MOPANI and sGMOPANI exhibit ideal rectangular shapes at low scanning rates (2 and 5 mV s^{-1}), reflecting the excellent double-layer capacitive and electrochemical reversibility. Furthermore, the CV profile of MOPANI deviates seriously from rectangularity and transform into spindle shape with increasing scanning rates, which is ascribed to poor electrical conductivity and severe aggregation of MOPANI. In contrast, sGMOPANI presents close-rectangular CV curves over in wide range of scanning rates (2–100 mV s^{-1}). This is because MOPANI nanoparticles deposit onto the surface of sGNS and increase the contacting area to the electrolyte, which is beneficial to ionic transport. Furthermore, the existence of sGNS facilitates charge transfer to the MnO$_2$ phase with poor conductivity.

To further investigate the influence of scanning rates on the capacitive character of MOPANI and sGMOPANI, the relationship of capacitance retention versus scanning rate is given in Fig. 7(C). As shown in Fig. 7(C), the capacitance retention of two composites

Table 1
The element content and chemical composition of MOPANI and sGMOPANI.

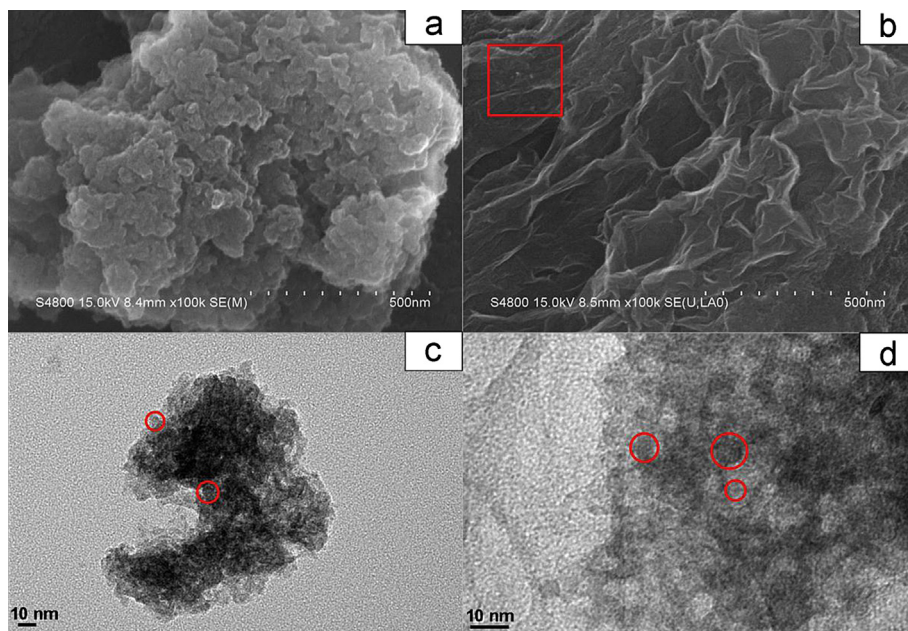| Samples	C (%)	O (%)	Mn[a] (%)	N (%)	S (%)	Composition[a]
MOPANI	41.9	34.5	17.1	6.5	0	MnO$_2$:PANI = 71:29
sGMOPANI	65.9	19.1	8.7	5.6	0.7	MnO$_2$:PANI:sGNS = 45:31:24

[a] The weight ratio.

Fig. 3. FE-SEM images of (a) MOPANI and (b) sGMOPANI. HRTEM images of (c) MOPANI and (d) sGMOPANI composites.

declines with increasing scanning rate. sGMOPANI maintains 57.7% of its capacitance as scanning rate rises from 2 to 100 mV s^{-1}, while MOPANI retains only 21.6% of its capacity in the same condition, demonstrating that the sGMOPANI has better rate capability.

As shown in Fig. 8(A), the galvanostatic charge/discharge curve of sGMOPANI is linear and symmetric, which is characteristic of an ideal capacitor capable of reversible charging and discharging. In comparison, the curve of MOPANI is distorted to some extent. Furthermore, the IR drop (marked in Fig. 8(A)) of sGMOPANI is much lower than that of MOPANI, indicating that the introduction of sGNS reduces significantly internal resistance. Low internal resistance is very favorable in energy-storage devices, which

reduce energy waste during charging/discharging processes. The specific capacitances of MOPANI and sGMOPANI are 276 F g^{-1} and 228 F g^{-1} at a current density of 1 A g^{-1}, respectively. This indicates that the specific capacitance of sGMOPANI is higher than that of MOPANI.

The rate capability of MOPANI and sGMOPANI is also evaluated by charging/discharging at different current densities (Fig. 8(B)). The sGMOPANI maintains its 73% capacitance (214 F g^{-1}) as the current density is increased from 0.2 to 20 A g^{-1}, while the MOPANI lost 68% of its capacity in the same condition, indicating that the sGMOPANI has better rate capability. This result is in good accordance with the CV tests.
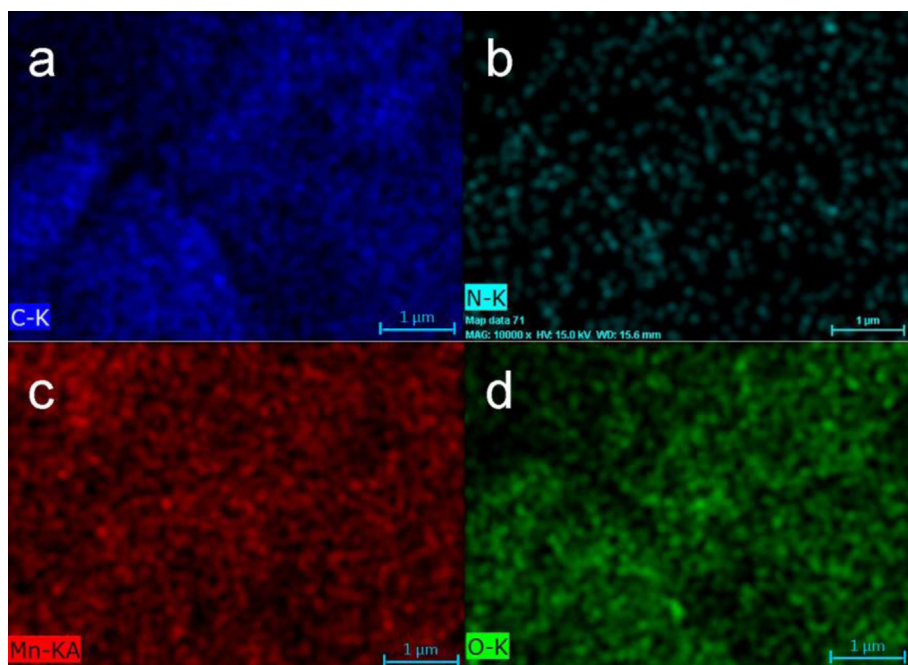

Fig. 4. Energy dispersive spectroscopic (EDS) analysis of sGMOPANI. (a) EDS carbon mapping, (b) EDS nitrogen mapping, (c) EDS manganese mapping, (d) EDS oxygen mapping.
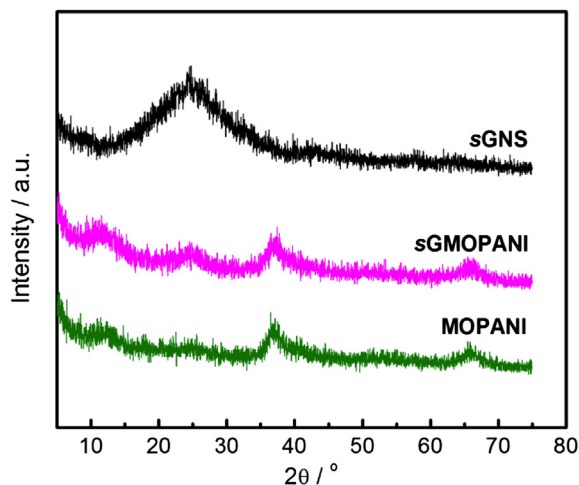
Fig. 5. XRD patterns of MOPANI and sGMOPANI.

The cycling stability of MOPANI and sGMOPANI in 1.0 M Na$_2$SO$_4$ electrolyte at a current density of 1 A g^{-1} is shown in Fig. 9(A). The specific capacitance of MOPANI decreases gradually with increasing cycle numbers and its capacitance retention is only 36.4% after 3000 cycles. By contrast, sGMOPANI lost 6.7% of its capacitance in
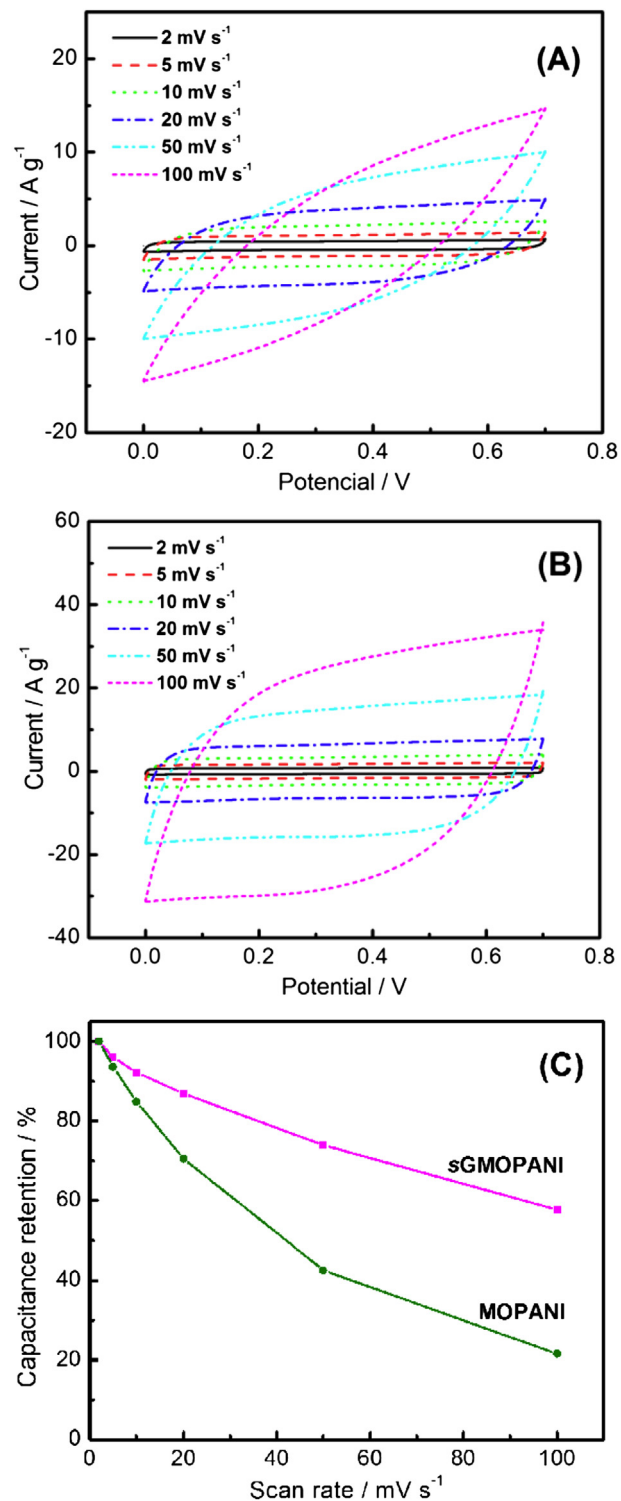

Fig. 6. (A) The N$_2$ adsorption/desorption isotherms and (B) pore size distributions of MOPANI and sGMOPANI.

Fig. 7. Cyclic voltammograms of (A) MOPANI and (B) sGMOPANI in 1 M Na$_2$SO$_4$ at different scan rates ranging from 2 to 100 mV s^{-1}. (C) The capacitance retention as a function of the scan rates for MOPANI and sGMOPANI.

the initial 500 cycles, and then only a little fading can be observed and the capacitance retention is 88.3% after 3000 cycles. This indicates that the cycling stability of sGMOPANI is significantly improved due to the introduction of sGNS.

EIS test was conducted for MOPANI and sGMOPANI before and after 3000 cycles to further study the cycling stability. As presented
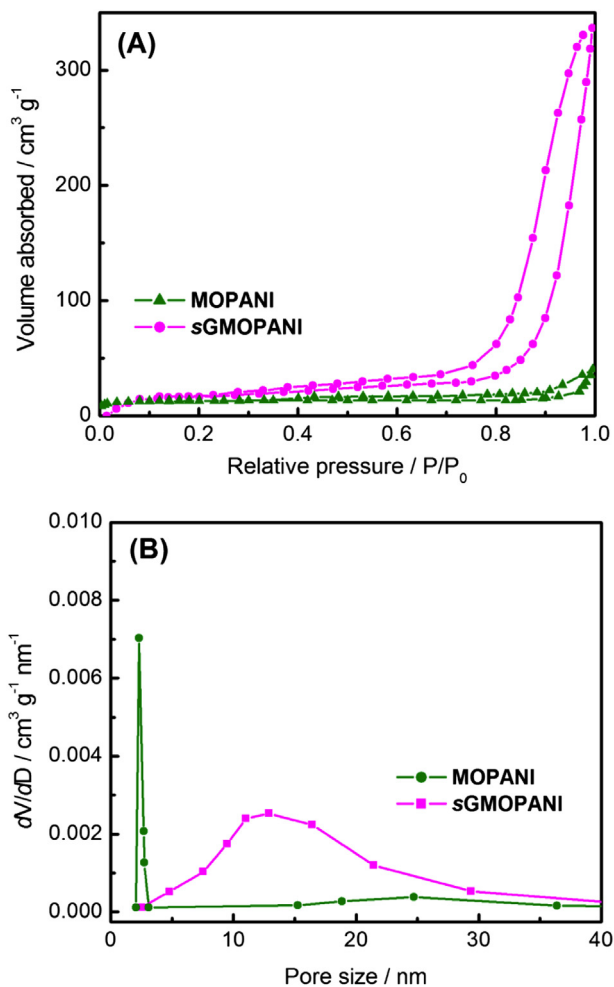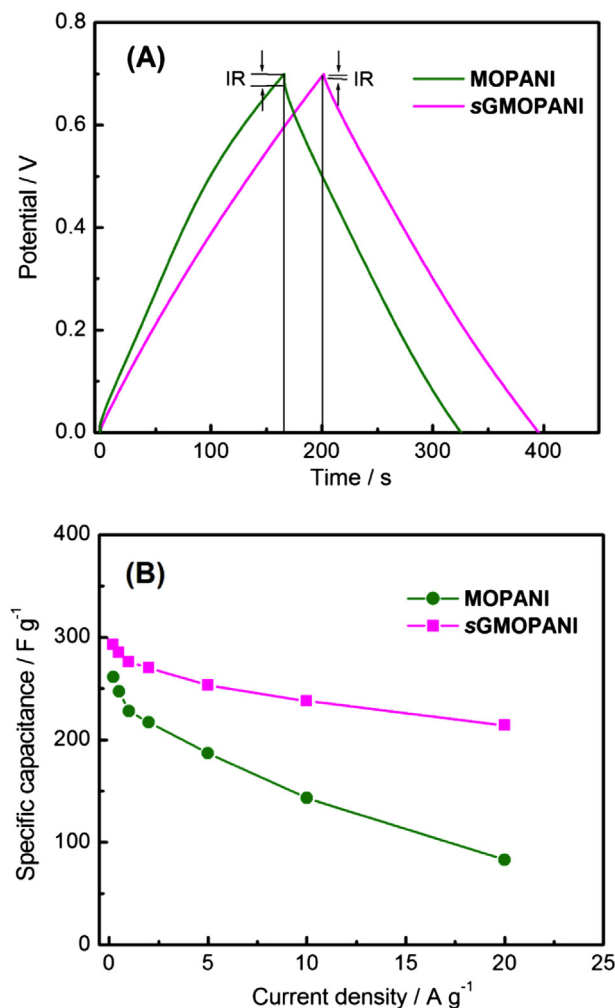
Fig. 8. (A) Galvanostatic charge/discharge curves in 1 M Na_2SO_4 at a current density of 1 A g^{-1} and (B) plots of the specific capacitance versus the discharging current densities for supercapacitors based on MOPANI and sGMOPANI.

Fig. 9. (A) Cycling stability for supercapacitors based on MOPANI and sGMOPANI in 1 M Na_2SO_4 at a current density of 1 A g^{-1} and (B) Nyquist plots for supercapacitors based on MOPANI and sGMOPANI in the frequency range of 100 kHz–0.01 Hz before cycling and after 3000 cycles.

in Fig. 9(B), during the initial cycling, two composites exhibit the impedance plots increasing sharply which tend to become vertical lines in the low-frequency region, indicating pure capacitive behavior. At the high frequencies, semi-circles can be observed for both with the diameters representing the charge-transfer resistance (R_{ct}). It is apparent that sGMOPANI has a much smaller R_{ct} than that of MOPANI. After cycling for 3000 times, the R_{ct} of MOPANI and sGMOPANI increase from 9.8 and 7.4 Ω to 17.1 and 10.0 Ω, respectively. This result reflects that the increasing rate of R_{ct} of the former is much higher than that of the latter. Moreover, the plot of MOPANI in the low-frequency region shows an obvious tendency to incline toward the real axis while sGMOPANI almost maintain the inclination angle, displaying the excellent pure capacitance characteristic even after 3000 cycles. EIS analytical results further support the conclusion that sGMOPANI exhibits good cycling stability compared with MOPANI, which is attributed to following three factors. Firstly, the MnO_2 and PANI components firmly deposited onto sGNS with exceptional mechanical performance through the π–π interaction and the hydrogen bonds. Secondly, the introduction of sGNS prevents further aggregation of the MnO_2/PANI nanoparticles, so the volume expansion and structure destruction of the electrode can be reduced during charge–discharge cycling. Finally, PANI thin layer on the surface of MnO_2 acts as a buffer to suppress the destruction of MnO_2 structure.
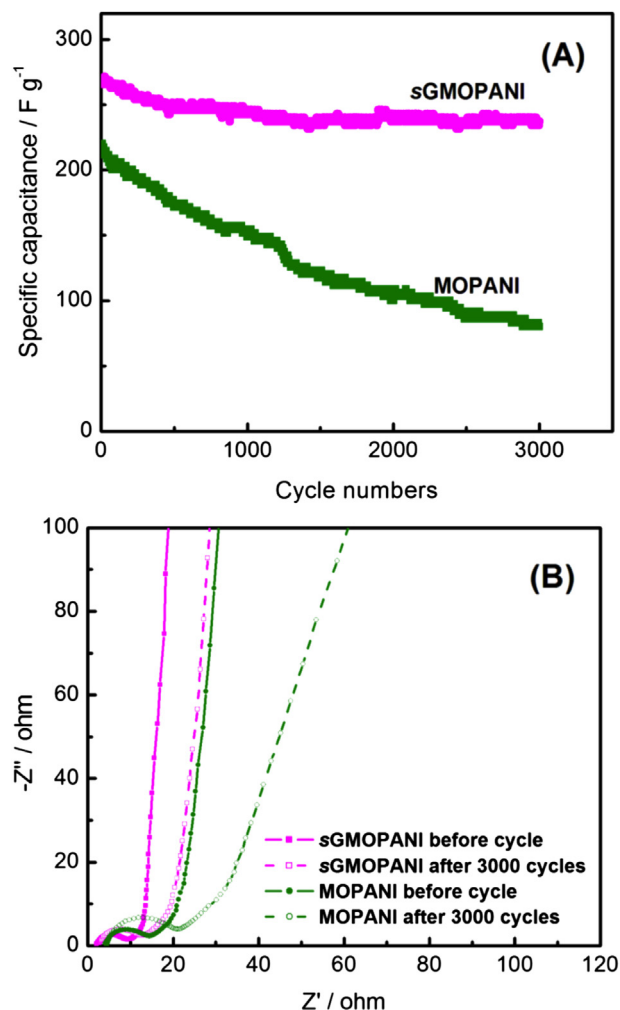
4. Conclusions

In summary, we have successfully synthesized hierarchical sulfonated graphene/MnO_2/polyaniline (sGMOPANI) ternary composite by a dilute in-situ polymerization method. The structural studies revealed that there are interactions between MnO_2/polyaniline composite nanoparticles and sulfonated graphene in sGMOPANI, such as hydrogen bonding and π–π stacking. It was also found that the sGNS not only provided high surface area for the deposition of MnO_2/polyaniline composite nanoparticles but also improved the electrical conductivity. The supercapacitors based on sGMOPANI electrodes showed a high specific capacitance of 276 F g^{-1} at a discharge current density of 1 A g^{-1} in 1 M Na_2SO_4 aqueous solution. Moreover, the sGMOPANI electrode exhibited a good cycling stability and rate capability. Therefore, the ternary composite is very promising in supercapacitors as well as other power source systems.

References

[1] P. Simon, Y. Gogotsi, Nat. Mater. 7 (2008) 845–854.
[2] H. Jiang, L. Yang, C. Li, C. Yan, P.S. Lee, J. Ma, Energy Environ. Sci. 4 (2011) 1813–1819.
[3] G. Yu, L. Hu, M. Vosgueritchian, H. Wang, X. Xie, J.R. McDonough, X. Cui, Y. Cui, Z. Bao, Nano Lett. 11 (2011) 2905–2911.
[4] B.E. Conway, Electrochemical Supercapacitors, Scientific Fundamentals and Technological Applications, Kluwer Academic/Plenum Press, New York, 1999.
[5] J.R. Miller, P. Simon, Science 321 (2008) 651–652.
[6] L.L. Zhang, X.S. Zhao, Chem. Soc. Rev. 38 (2009) 2520–2531.
[7] E. Raymundo-Pinero, F. Leroux, F. Beguin, Adv. Mater. 18 (2006) 1877–1883.
[8] M. Kaempgen, C.K. Chan, J. Ma, Y. Cui, G. Gruner, Nano Lett. 9 (2009) 1872–1876.
[9] M.F. El-Kady, V. Strong, S. Dubin, R.B. Kaner, Science 335 (2012) 1326–1330.
[10] K.S. Ryu, K.M. Kim, N.G. Park, Y.J. Park, S.H. Chang, J. Power Sources 103 (2002) 305–309.
[11] B.K. Kuila, B. Nandan, M. Bohme, A. Janke, M. Stamm, Chem. Commun. (2009) 5749–5751.
[12] C.C. Hu, K.H. Chang, M.C. Lin, Y.T. Wu, Nano Lett. 6 (2006) 2690–2695.
[13] H.L. Wang, H.S. Casalongue, Y.Y. Liang, H.J. Dai, J. Am. Chem. Soc. 132 (2010) 7472–7477.
[14] H. Jiang, T. Zhao, C.Z. Li, J. Ma, J. Mater. Chem. 21 (2011) 3818–3823.
[15] M. Toupin, T. Brousse, D. Belanger, Chem. Mater. 16 (2004) 3184–3190.
[16] K.W. Nam, C.W. Lee, X.Q. Yang, B.W. Cho, W.S. Yoon, K.B. Kim, J. Power Sources 188 (2009) 323–331.
[17] Y. Hou, Y.W. Cheng, T. Hobson, J. Liu, Nano Lett. 10 (2010) 2727–2733.
[18] T. Shinomiya, V. Gupta, N. Miura, Electrochim. Acta 51 (2006) 4412–4419.
[19] H. Xia, J.K. Feng, H.L. Wang, M.O. Lai, L. Lu, J. Power Sources 195 (2010) 4410–4413.
[20] H.S. Nam, J.K. Yoon, J.M. Ko, J.D. Kim, Mater. Chem. Phys. 123 (2010) 331–336.
[21] O.A. Vargas, A. Caballero, L. Hernan, J. Morales, J. Power Sources 196 (2011) 3350–3354.
[22] H.Q. Wang, G.F. Yang, Q.Y. Li, X.X. Zhong, F.P. Wang, Z.S. Li, Y.H. Li, New J. Chem. 35 (2011) 469–475.
[23] H.Q. Wang, Z.Q. Li, J.M. Ma, C.Y. Yan, C.Z. Li, Chem. Commun. 47 (2011) 1264–1266.
[24] X.H. Tang, H.J. Li, Z.H. Liu, Z.P. Yang, Z.L. Wang, J. Power Sources 196 (2011) 855–859.
[25] P.C. Gao, A.H. Lu, W.C. Li, J. Power Sources 196 (2011) 4095–4101.
[26] S.B. Ma, K.W. Nam, W.S. Yoon, X.Q. Yang, K.Y. Ahn, K.H. Oh, K.B. Kim, J. Power Sources 178 (2008) 483–489.
[27] L. Li, Z.Y. Qin, L.F. Wang, H.J. Liu, M.F. Zhu, J. Nanopart. Res. 12 (2010) 2349–2353.
[28] L.B. Hu, W. Chen, X. Xie, N.A. Liu, Y. Yang, H. Wu, Y. Yao, M. Pasta, H.N. Alshareef, Y. Cui, ACS Nano 5 (2011) 8904–8913.
[29] P. Lv, P. Zhang, Y.Y. Feng, Y. Li, W. Feng, Electrochim. Acta 78 (2012) 515–523.
[30] H.J. Zheng, J.X. Wang, Y. Jia, C.A. Ma, J. Power Sources 216 (2012) 508–514.
[31] J. Yan, Z.J. Fan, T. Wei, W.Z. Qian, M.L. Zhang, F. Wei, Carbon 48 (2010) 3825–3833.
[32] G.H. Yu, L.B. Hu, N.A. Liu, H.L. Wang, M. Vosgueritchian, Y. Yang, Y. Cui, Z.A. Bao, Nano Lett. 11 (2011) 4438–4442.
[33] Q. Cheng, J. Tang, J. Ma, H. Zhang, N. Shinya, L.C. Qin, Carbon 49 (2011) 2917–2925.
[34] L. Mao, K. Zhang, H.S.O. Chan, J.S. Wu, J. Mater. Chem. 22 (2012) 1845–1851.
[35] C.Y. Chen, C.Y. Fan, M.T. Lee, J.K. Chang, J. Mater. Chem. 22 (2012) 7697–7700.
[36] F.J. Liu, J. Power Sources 182 (2008) 383–388.
[37] X.F. Yang, G.C. Wang, R.Y. Wang, X.W. Li, Electrochim. Acta 55 (2010) 5414–5419.
[38] L. Chen, L.J. Sun, F. Luan, Y. Liang, Y. Li, X.X. Liu, J. Power Sources 195 (2010) 3742–3747.
[39] J.G. Wang, Y. Yang, Z.H. Huang, F.Y. Kang, J. Power Sources 204 (2012) 236–243.
[40] H. Jiang, J. Ma, C. Li, J. Mater. Chem. 22 (2012) 16939–16942.
[41] R.K. Sharma, A.C. Rastogi, S.B. Desu, Electrochim. Acta 53 (2008) 7690–7695.
[42] R.K. Sharma, A. Karakoti, S. Seal, L. Zhai, J. Power Sources 195 (2010) 1256–1262.
[43] R. Liu, J. Duay, S.B. Lee, ACS Nano 4 (2010) 4299–4307.
[44] R. Liu, S.B. Lee, J. Am. Chem. Soc. 130 (2008) 2942–2943.
[45] S.R. Sivakkumar, J.M. Ko, D.Y. Kim, B.C. Kim, G.G. Wallace, Electrochim. Acta 52 (2007) 7377–7385.
[46] C.Z. Yuan, L.H. Su, B. Gao, X.G. Zhang, Electrochim. Acta 53 (2008) 7039–7047.
[47] Q.A. Li, J.H. Liu, J.H. Zou, A. Chunder, Y.Q. Chen, L. Zhai, J. Power Sources 196 (2011) 565–572.
[48] Y.F. Yan, Q.L. Cheng, V. Pavlinek, P. Saha, C.Z. Li, Electrochim. Acta 71 (2012) 27–32.
[49] J.-G. Wang, Y. Yang, Z.-H. Huang, F. Kang, J. Mater. Chem. 22 (2012) 16943–16949.
[50] J. An, J. Liu, Y. Ma, R. Li, M. Li, M. Yu, S. Li, Eur. Phys. J. Appl. Phys. 58 (2012) 30403–30411.
[51] A.K. Geim, K.S. Novoselov, Nat. Mater. 6 (2007) 183–191.
[52] J.R. Miller, R.A. Outlaw, B.C. Holloway, Science 329 (2010) 1637–1639.
[53] Y. Zhu, S. Murali, M.D. Stoller, K.J. Ganesh, W. Cai, P.J. Ferreira, A. Pirkle, R.M. Wallace, K.A. Cychosz, M. Thommes, D. Su, E.A. Stach, R.S. Ruoff, Science 332 (2011) 1537–1541.
[54] Y. Si, E.T. Samulski, Nano Lett. 8 (2008) 1679–1682.
[55] L. Jin, G. Wang, X. Li, L. Li, J. Appl. Electrochem. 41 (2011) 377–382.
[56] J. Yan, Z.J. Fan, T. Wei, J. Cheng, B. Shao, K. Wang, L.P. Song, M.L. Zhang, J. Power Sources 194 (2009) 1202–1207.
[57] Z.P. Li, Y.J. Mi, X.H. Liu, S. Liu, S.R. Yang, J.Q. Wang, J. Mater. Chem. 21 (2011) 14706–14711.
[58] C.J. Xu, B.H. Li, H.D. Du, F.Y. Kang, Y.Q. Zeng, J. Power Sources 184 (2008) 691–694.
[59] Z.S. Wu, W.C. Ren, D.W. Wang, F. Li, B.L. Liu, H.M. Cheng, ACS Nano 4 (2010) 5835–5842.